Mechanically controllable nonlinear dielectrics

Ko, D. L.; Tsai, M. F.; Chen, J. W.; Shao, P. W.; Tan, Y. Z.; Wang, J. J.; Ho, S. Z.; Lai, Y. H.; Chueh, Y. L.; Chen, Y. C.; Tsai, D. P.; Chen, L.-Q.; Chu, Y. H.

Published in:
Science Advances

Published: 01/03/2020

Document Version:
Final Published version, also known as Publisher's PDF, Publisher's Final version or Version of Record

Published version (DOI):
10.1126/sciadv.aaz3180

Publication details:
Ko, D. L., Tsai, M. F., Chen, J. W., Shao, P. W., Tan, Y. Z., Wang, J. J., Ho, S. Z., Lai, Y. H., Chueh, Y. L., Chen, Y. C., Tsai, D. P., Chen, L-Q., & Chu, Y. H. (2020). Mechanically controllable nonlinear dielectrics. *Science Advances*, *6*(10), [eaaz3180]. https://doi.org/10.1126/sciadv.aaz3180

MATERIALS SCIENCE

Mechanically controllable nonlinear dielectrics

D. L. Ko[1], M. F. Tsai[1], J. W. Chen[2], P. W. Shao[1], Y. Z. Tan[3], J. J. Wang[3], S. Z. Ho[2], Y. H. Lai[1], Y. L. Chueh[4,5], Y. C. Chen[2], D. P. Tsai[6,7], L.-Q. Chen[3], Y. H. Chu[1,8,9]*

Strain-sensitive $Ba_xSr_{1-x}TiO_3$ perovskite systems are widely used because of their superior nonlinear dielectric behaviors. In this research, new heterostructures including paraelectric $Ba_{0.5}Sr_{0.5}TiO_3$ (BSTO) and ferroelectric $BaTiO_3$ (BTO) materials were epitaxially fabricated on flexible muscovite substrate. Through simple bending, the application of mechanical force can regulate the dielectric constant of BSTO from −77 to 36% and the channel current of BTO-based ferroelectric field effect transistor by two orders. The detailed mechanism was studied through the exploration of phase transition and determination of band structure. In addition, the phase-field simulations were implemented to provide theoretical support. This research opens a new avenue for mechanically controllable components based on high-quality oxide heteroepitaxy.

INTRODUCTION

In solids, the periodic configuration of atoms is a consequence of energy minimization. The involved atoms and corresponding arrangements determine the properties of materials. Therefore, dynamically tuning the periodicity of atom arrangements, or strain application, is a fundamental approach to tune the functionalities of materials. According to the literature, several approaches have been developed to impose strain on materials. As early as the 1970s, scientists have applied a hydrostatic pressure (*1*–*3*) (up to 70 kbar) to the Fe_2SiO_4 lattice and observed the shift of diffraction peaks through x-ray analysis, delivering a direct evidence of lattice alteration by external force. Moreover, external stimuli such as magnetic field, electric field, and light illumination can also induce a change of lattice attributed to the effects of magnetostriction, electrostriction, and photostriction. For instance, a giant magnetic field is widely used to change the lattice of Heusler alloys (*4*–*6*) to trigger magnetic shape memory effect, and electric field is commonly applied to alter the phases of ferroelectric materials such as $PbTiO_3$-based (*7*) and $BiFeO_3$-based (*8*) materials, resulting in large piezoelectric effects. The phenomenon of photostriction is widely observed in various types of materials such as ferroelectrics, polar and nonpolar semiconductors, and organic-based materials (*9*), leading to a size alteration of samples. However, currently, there is no applicable method to apply mechanical force to materials since the application of hydrostatic pressure cannot be implemented in a device form. This concept in principle can be realized by mechanical bending because it is the simplest way to cause material deformation. Such a method requires the mechanical flexibility of materials. Besides, to ensure that the strain can be imposed without the absorption by defect formation, high-quality materials such as single crystals or epitaxial films are preferred. However, most single crystals cannot be bent mechanically. Thus, there are two critical requirements for the desired architecture: high mechanical flexibility (*10*) and the ability of epitaxial growth (*11*). In search of suitable substrate to build up heterostructures, two-dimensional (2D) layered oxide muscovite (*12*) is an eligible candidate due to the fact that it has superior mechanical flexibility with high melting point (~1260° to 1290°C). In the past researches, the capability of epitaxial growth on muscovite via van der Waals epitaxy has been demonstrated on various kinds of materials (*13*–*16*) with excellent mechanical flexibility. To acquire the modulation of material properties, functional material with large strain susceptibility is needed. Among them, nonlinear dielectric material is selected because of the strong coupling between lattice structure and properties, such as dielectric constant and ferroelectric polarization (*17*). If a strain can be applied to the lattice, then it can change the ability of charge storage and the magnitude of ferroelectric polarization. In this way, signals can be controlled in an electrical component by mechanical bending, delivery of a simple method to control material properties, and modulation of corresponding device functionalities (*18*). Among traditional nonlinear dielectrics, nontoxic perovskite $Ba_xSr_{1-x}TiO_3$ systems (*19*–*20*) show high sensitivity to strain application. Thus, in this study, paraelectric $Ba_{0.5}Sr_{0.5}TiO_3$ (BSTO) and ferroelectrics $BaTiO_3$ (BTO) were selected as model systems to exhibit the control by mechanical bending.

Typically, a strain can be applied to perovskite lattice through the fabrication on a substrate with lattice mismatch or a change of process temperature to tune its ground state permanently (*21*). However, in our demonstration, we show the ability of dynamically tuning ferroelectric-to-paraelectric phase transition of $Ba_xSr_{1-x}TiO_3$ system to modulate the corresponding dielectric and ferroelectric properties via mechanical bending. In addition to the bending study of BTO and BSTO capacitors, a focus on the application of this effect was carried out. A ferroelectric field effect transistor (FeFET) (*22*–*24*) with the mechanically controllable feature was built up on the basis of BTO with high-mobility Al-doped ZnO (AZO) (*25*–*27*) as a semiconductor layer. Capacitance-voltage (CV), polarization-voltage (PV), and current-voltage (IV) measurements were used to characterize the dielectric constant of BSTO, the ferroelectric properties of BTO, and the channel current of FeFET, respectively, to study the bending effect on BSTO capacitor and BTO FeFET. The change of lattice under bending can be observed through Raman spectroscopy. X-ray photoelectron spectroscopy (XPS) was used to highlight the influence of BTO

[1]Department of Materials Science and Engineering, National Chiao Tung University, Hsinchu 30010, Taiwan. [2]Department of Physics, National Cheng Kung University, Tainan 70101, Taiwan. [3]Department of Materials Science and Engineering, Pennsylvania State University, University Park, PA 16802, USA. [4]Department of Materials Science and Engineering, National Tsing Hua University, Hsinchu 30013, Taiwan. [5]Frontier Research Center on Fundamental and Applied Sciences of Matters, National Tsing Hua University, Hsinchu 30013, Taiwan. [6]Research Center for Applied Sciences, Academia Sinica, Taipei 11529, Taiwan. [7]Department of Electronic and Information Engineering, Hong Kong Polytechnic University, Kowloon Hong Kong. [8]Institute of Physics, Academia Sinica, Taipei 11529, Taiwan. [9]Center for Emergent Functional Matter Science, National Chiao Tung University, Hsinchu 30010, Taiwan.
*Corresponding author. Email: yhc@nctu.edu.tw

polarization on the electronic structure in the semiconductor AZO layer under different bending conditions.

RESULTS

As shown in the schematics of Fig. 1A, both BSTO capacitor and BTO FeFET systems were fabricated on muscovite substrates. Epitaxial AZO, BSTO, and BTO layers were built on (001) native muscovite with epitaxial $SrRuO_3$ (SRO) layer as the bottom electrode. Perovskite SRO is a suitable electrode because it presents a small lattice misfit to BTO, superior chemical compatibility, and good metallicity. To promote the SRO growth on muscovite, a seeding layer of $CoFe_2O_4$ (CFO) was inserted (*28*). All these advantages lead to the feature of heteroepitaxy on muscovite with superior crystallinity. Figure 1B displays the heterostructure of AZO/BTO/SRO/CFO/muscovite grown by pulsed laser deposition. The details of growth conditions can be found in Materials and Methods. The structural characteristics were examined by x-ray diffraction. Figure 1C shows a typical out-of-plane θ-2θ scan of the AZO/BTO/SRO/CFO/muscovite heterostructure. Only muscovite (00 *L*), AZO(00 *L*), BTO(111), and SRO(111) diffraction peaks were detected, indicating high crystalline quality of the heterostructure without secondary phases. However, the thickness of the CFO seeding layer is too thin to detect. The crystal quality of each layer was characterized by the rocking curve measurement that uses a tiny swinging ω angle to scan the heterostructure. The critical information of crystallinity was obtained and resulted in the full width at half maximum of ~4°, ~2.4°, and ~1.4° for AZO(002), BTO(111), and SRO(222) peaks (Fig. 1D), respectively. Furthermore, the Φ-scans of AZO(101), SRO(002), BTO(002), and muscovite (202) were used to determine the in-plane orientation relationship as shown in Fig. 1E. Muscovite (202) originally presents a twofold symmetry due to its monoclinic tilting angle between *a* and *c* axes (β = 100°). Therefore, the observation of three muscovite (202) peaks at every 120° intervals indicated that there are three different configurations corresponding to an alternating stacking sequence of muscovite. A similar result can be observed on BTO(002) as well. Perovskite BTO has a threefold symmetry along the (111) orientation, and thus the presence of six peaks in the Φ-scan of (002) at 60° intervals revealed the coexistence of two sets of domains in the BTO layer. The top semiconductor AZO layer is a hexagonal wurtzite structure that has a sixfold symmetry along the (002) orientation, so the presence of 12 peaks in the Φ-scan of (101) at 30° intervals revealed the coexistence of two sets of domains in the AZO layer. On the basis of the XRD results, the epitaxial relationship of the heterostructure can be determined as $(002)_{AZO}//(111)_{BTO}//(111)_{SRO}//(001)_{Mica}$ and $[010]_{AZO}//[1\text{-}10]_{BTO}//[1\text{-}10]_{SRO}//[010]_{Mica}$, as shown in the schematic of Fig. 1B. To examine the microstructure and interface quality on the heteroepitaxy of AZO/BTO/SRO/CFO/mica, we characterized the interfaces of the heterostructure by high-resolution transmission electron microscopy (TEM). Figure 1F shows the cross-sectional TEM images taken along $[010]_{Mica}$ zone axis, revealing sharp AZO/BTO, BTO/SRO, and SRO/CFO/Mica interfaces. The reciprocal lattices of the selected area diffraction patterns of AZO, BTO, SRO, and mica were clearly indexed. The consistency of epitaxial relationships with the XRD results is confirmed. On the basis of the results of XRD and TEM, a superior heteroepitaxy was delivered. Since BSTO is a solid solution of BTO and $SrTiO_3$ (STO), the similar structural information was obtained for BSTO system, and the corresponding information is included in the Supplementary Materials (fig. S1).

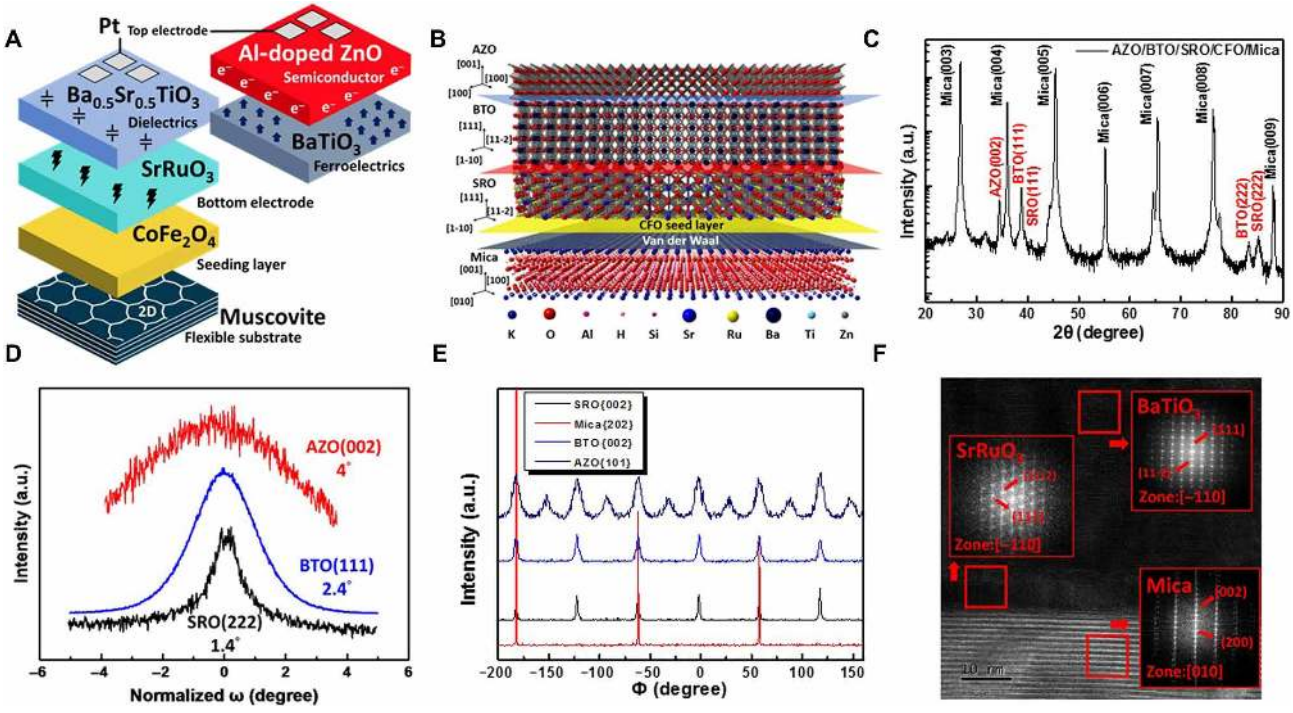

Fig. 1. Structural characteristics of heteroepitaxy. (**A**) Schematic of BSTO and BTO systems. (**B**) Schematic of the epitaxial relationship. (**C**) Out-of-plane x-ray 2θ-θ scan of the heterostructure. a.u., arbitrary units. (**D**) Rocking curves of SRO(222), BTO(111), and AZO(002). (**E**) Φ-Scan of muscovite{202}, SRO{002}, BTO{002}, and AZO{101}. (**F**) Cross-sectional TEM image at the interface and the corresponding fast Fourier transform (FFT) patterns in the insets.

To ensure the application of strain by mechanical bending, we used muscovite substrate since they are mechanically flexible. Before the fabrication of heterostructure, a detailed analysis on the mechanical flexibility of muscovite substrate was performed. On the premise that no visible cracks or wrinkles on the surface of muscovite substrates can be found under the examination of optical microscope, we accumulated the experience of peeling layered muscovite substrate repeatedly and plotted the relationship between muscovite thickness and bending curvature. The result is shown in Fig. 2A, the *y* and *x* axes represent the thickness of muscovite substrate (millimeter) and the bending curvature (per millimeter), respectively. This result shows that the thinner the muscovite substrate is, the better the bending ability. In this study, the maximum of curvature is 0.285 mm^{-1}, so the thickness of muscovite substrate was fixed at ~0.015 mm to ensure that the component was still intact after many bending cycles.

Since the epitaxial feature has been confirmed, the attention now is paid to physical characteristics of the heterostructure. The key hypothesis is that through the mechanical bending, the strain can be imposed on the perovskite layer resulting in changes of BTO ferroelectricity and dielectric constant of BSTO. Thus, CV and PV measurements were carried out to characterize electrical properties under various bending conditions. For the BSTO heterostructure (200 nm in thickness), an electric field ranging from −300 to 300 kV/cm was scanned. At room temperature, uniformly mixed by BTO and STO,

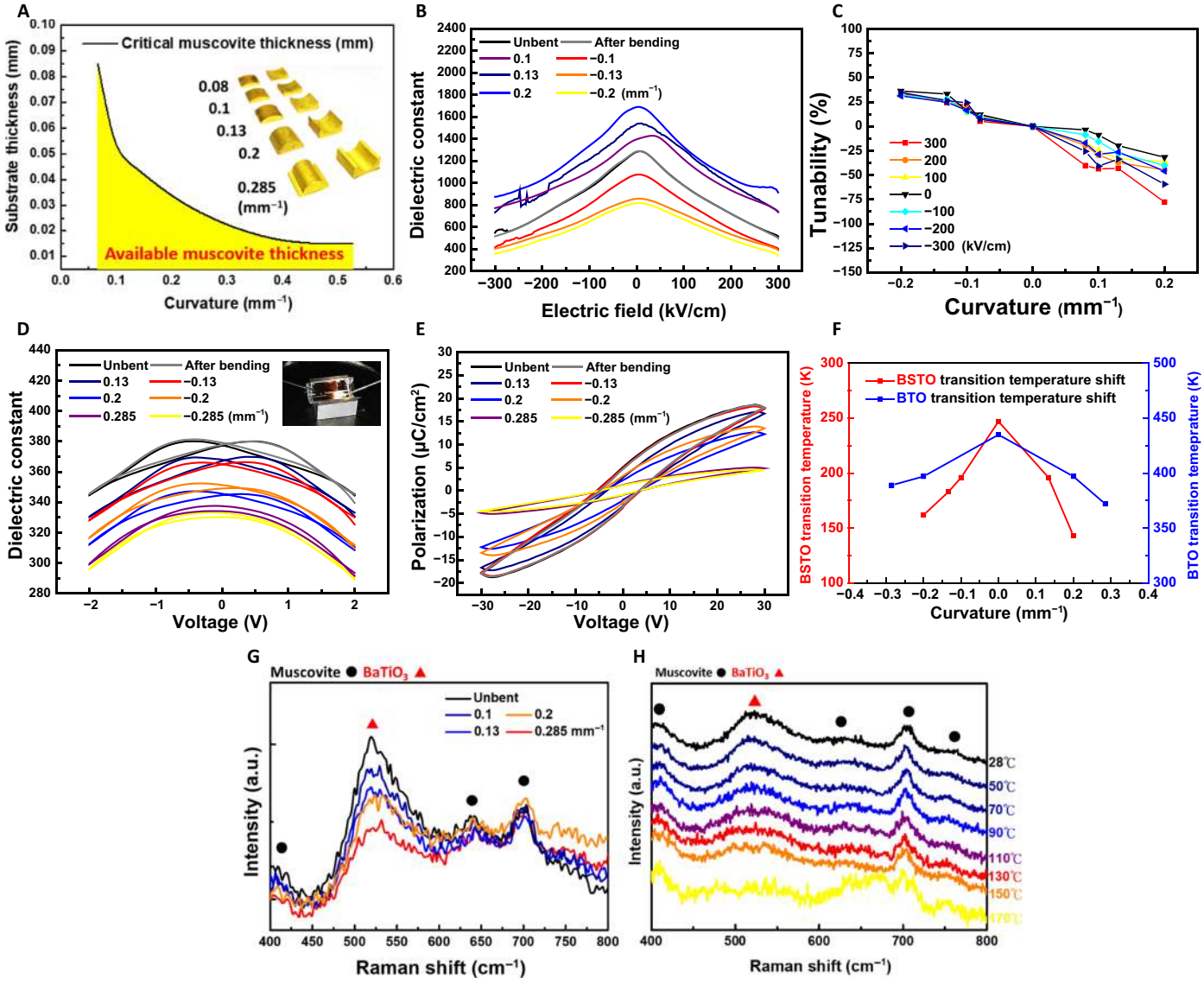

Fig. 2. Ferroelectric properties. (**A**) The relationship between curvature and thickness of muscovite substrate. (**B**) The dielectric constant of BSTO under different bending curvatures. (**C**) The tunability of varied electric field under different bending curvatures. (**D**) *C-V* butterfly shape at unbent state and dielectric constant at different bending states. (**E**) Polarization-voltage hysteresis loops at various tensile and compressive bending curvatures. Credit: Deng Li Ko, Department of Materials Science and Engineering, National Chiao Tung University, Hsinchu 30010, Taiwan. (**F**) The transition temperature of BSTO and BTO under different bending curvatures. (**G**) The amplitude of Raman signal at unbent and bent curvatures of 0.1, 0.13, 0.2, and 0.285 mm^{-1}. (**H**) Raman spectra of the heterostructure at the temperature ranging from room temperature to 170°C.

the Curie temperature of BSTO film was approximately −30°C in the middle of the Curie point of BTO and the phase transition temperature of STO (105 K), presenting a paraelectric state. From the CV result, single peak appears at the zero electric field position. At unbent state (black line in Fig. 2B), the dielectric constant can be regulated from 513 to 1280 when the electric field is applied between −300 and 300 kV/cm (Fig. 2B). On the basis of the conventional definition, the electrical tunability of BSTO capacitor is about 60 to 70%. This value is consistent with those found in the literatures (*29*), confirming high quality of the heterostructure. Unexpectedly, except regulated by electric field, the dielectric constant was raised and declined under the positive and negative bending curvatures. According to the result, a systematic change of BSTO dielectric constant under mechanical bending was observed. The tunability of dielectric constant under bending was defined as the formula

$$\text{Tunability (\%)} = \frac{\varepsilon_r(\text{Unbent}) - \varepsilon_r(\text{Bending})}{\varepsilon_r(\text{Unbent})}$$

where ε_r(Unbent) is the permittivity without mechanical bending and ε_r(Bending) is the permittivity under mechanical bending.

This formula compares the status of unbent and bending and highlights the ratio of dielectric constant change. The change of dielectric constant as a function of curvature was extracted and shown in Fig. 2C. The dielectric constant of BSTO was altered nonlinearly from −77 to 36%. The sign of tunability depends on the bending modes. A flex-in mode (compressive strain) leads to a negative sign, and the flex-out mode (tensile strain) results in a positive change. This shows that the amount of charge that can be stored by this dielectric material can be tuned due to the stretching of lattice structure. The same experiment was carried out on the capacitor made of BTO layer. The results of CV measurement are shown in Fig. 2D. The dielectric constant of BTO layer was characterized to be approximately from 330 to 380 at a different bending curvature. However, more attention was paid to the ferroelectric behaviors. The black curve demonstrates a butterfly shape with double-peak feature that represents a ferroelectric state with an indication of the coercive field at 0.5 V. When a curvature of 0.2 mm^{-1} was achieved on this heterostructure, double peaks of the butterfly shape become closer, suggesting that the ferroelectric polarization was weakened. At the 0.285-mm^{-1} curvature, no matter under flex-in or flex-out bending, the butterfly double peaks were superimposed as a single peak, implying the transformation into a general paraelectric state. The corresponding phenomenon also appears in the PV measurement as shown in Fig. 2E. The black line is the result of the unbent state. The maximum saturated polarization is 18.8 μC/cm^2 and begins to decrease at the 0.13-mm^{-1} curvature. The saturated polarization is reduced to 5.14 μC/cm^2 at the 0.285-mm^{-1} curvature. A 72.6% change of the polarization was detected from the unbent state to the bending of 0.285-mm^{-1} curvature. According to the CV and PV results, it can be known that under mechanical bending, the ferroelectric state of BTO layer gradually disappears and turns into a paraelectric phase. All the behaviors can be restored after the heterostructure was flattened, indicating that the nonlinear dielectric properties are controllable and repeatable under mechanical bending, implying a great potential for practical applications.

To find more evidence on the bending effect, we carried out the temperature-dependent CV measurements under different bending curvatures to observe the alteration of the ferroelectric phase. It should be noticed that, in this temperature-dependent CV measurement, the polarization observed is along the out-of-plane direction. The critical temperature is called the transition temperatures of P_z in this study. According to the results (Fig. 2F), the transition temperature of BSTO (red line) was 247 K at the unbent state and changed to 143 K under the curvature of 0.2 mm^{-1}. On the BTO part (blue line), the transition temperature changed from 435 to 372 K under the curvature at 0.285 mm^{-1}. Whether it is tensile or compressive strain, the transition temperature of P_z was in a downward trend. This phenomenon suggested the transition temperature can be altered in both BSTO and BTO systems.

The phenomenon that mechanical bending can alternate ferroelectric properties was confirmed through multimeasurement. In tradition, temperature-dependent Raman spectroscopy is an excellent tool to study the phase transition of ferroelectric materials. From the previous studies, the Raman spectrum of BTO shows different intensity under varied lattice structures as a function of temperature (*30*–*31*). Thus, Raman spectroscopy on the heterostructure under mechanical bending was carried out. Among the vibration modes of BTO, the Raman shift located at 518 cm^{-1} represents a critical phonon vibration peak to determine the tetragonal phase of BTO. On the basis of the intensity of this peak, it can be estimated whether the BTO ferroelectric phase exists. In Fig. 2G, at the unbent state (black line), the signal of BTO tetragonal phase has a relatively strong intensity. While at the bending state, the peak intensity at 520 cm^{-1} was substantially reduced. The intensity of this peak became lower with an increase of the curvature, indicating the structure change of BTO lattice. The transformation from tetragonal to cubic structures directly leads to the weakening of the ferroelectric phase. More notable is that after the heterostructure was flattened, the peak value showed a significant rebound. Meanwhile, the Raman measurement at variable temperatures ranging from 28° to 170°C was implemented to observe the change of ferroelectric signature. As shown in Fig. 2H, the upper black line shows that the BTO layer at room temperature has a remarkable tetragonal structure. When the temperature rises between 130° and 170°C, the tetragonal structure begins to change into cubic, and the result is consistent to the one in the bending measurement. A more detailed analysis for the Raman results is included in fig. S2. Through this series of measurements, it can be confirmed that the BTO structure during the bending process can cause a structural transformation, leading to a reduction of the out-of-plane ferroelectric polarization. The Raman result highlights that the symmetry is increased during bending and leads to a decrease of the polarization. The result can be recovered to the flattened state after bending since the peak intensity can also return to the original state. This phenomenon delivers a direct evidence on the modulation of ferroelectric state by mechanical bending.

To further investigate the behaviors of BSTO and BTO layers under the mechanical bending, we have carried out a set of the phase-field simulations (*32*). Assuming that the bending radius is significantly larger than the thickness of the simulated system, a linear approximation can be used to describe the depth-dependent in-plane strain

$$\varepsilon'_{yy} = \frac{z + H/2}{R} \quad (1)$$

Where H and R represent the thickness of substrate and the bending radius, respectively. The direction of stretching or compressing is assigned along y direction. Such a distribution of external stress is illustrated in Fig. 3A.

For BSTO films, the simulated out-of-plane dielectric constant and tunability under positive and negative bending directions are shown

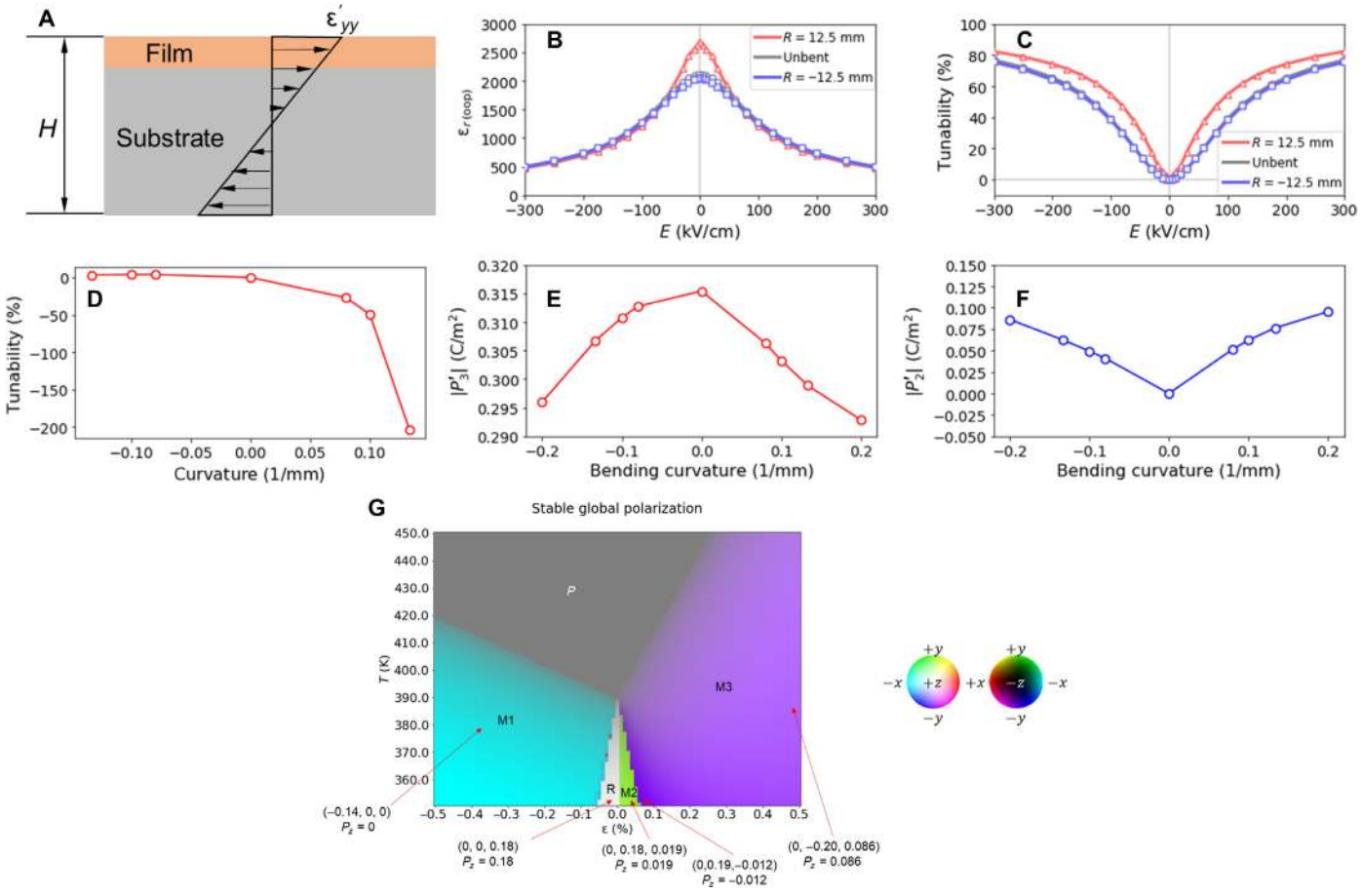

Fig. 3. Simulated results for BSTO and BTO ferroelectric properties under different bending conditions. (**A**) Illustration of externally applied strain distribution in the simulated systems. (**B**) Dielectric constants with different bending directions and electric fields for BSTO. (**C**) Tunability versus the applied electric fields for different bending directions for BSTO. (**D**) Tunability change for various bending curvatures for BSTO. (**E**) Magnitude of the polarization component along *z* direction ($|P_3'|$) with the DC bias $E_z = 80$ kV/cm. (**F**) Magnitude of the polarization component along *y* direction ($|P_2'|$) with the DC bias $E_z = 80$ kV/cm. (**G**) Phase diagram for the uniaxial bending case. Colors correspond to the most stable polarization directions. Gray represents the paraelectric phase.

in Fig. 3 (B and C), along with the change in tunability versus bending curvature shown in Fig. 3D. It could be seen from the results that different bending directions have opposite effects on tuning the magnitudes of out-of-plane permittivity and tunability. Bending with a positive curvature increases the permittivity, and negative curvatures correspond to decrease of permittivity, which shows the same tendency with the experimental results. For BTO films, simulations are carried out to study the change in polarization under a direct current (DC) bias $E_z = 80$ kV/cm with various bending curvatures. The results are illustrated in Fig. 3 (E and F). For all cases simulated, magnitudes of P_1' are negligible and not shown in the figures. It could be seen from the figure that the magnitude of out-of-plane component of polarization ($|P_3'|$) drops when bending curvature arises (i.e., when a smaller bending radius is applied), regardless of the bending direction, which also corresponds qualitatively to the tendency observed in the experiments. Thermodynamic calculations were performed to understand the decrease in the phase transition temperature under both flex-in and flex-out modes. Figure 3G shows the uniaxial strain versus temperature phase diagram, where the compressive and tensile uniaxial strains are induced by bending up and down the mica substrate, respectively. In the phase diagram, the ferroelectric phases under high-strain magnitudes (M1 and M3 phases) occupy a comparably low out-of-plane polarization component, while the most stable phases under low external strains (R and M2) come with a large out-of-plane polarization component. The reduced polarization component along *z* direction under large strains also indicates an enhanced symmetry along the out-of-plane direction. When finding the maxima of the out-of-plane dielectric constant in the experiments, only the *z* component of polarization can be monitored. The phase boundaries of M1 to R and M3 to M2 are defined by the emergence of *z* component of the polarization. As a result, the measured ε_{zz} maxima actually reflect the phase transitions from ferroelectric M1 to R and M3 to M2 rather than the paraelectric to ferroelectric phase transition. From the phase diagram, it can be seen that transition temperature of M1 to R decreases with compressive strain, and the transition temperature of M3 to M2 decreases with tensile strain. This explains that the experimentally observed transition temperatures of P_z are decreased for both flex-in and flex-out modes.

To show an amplification that the ferroelectric state of BTO layer can be changed to the paraelectric state, the semiconductor AZO

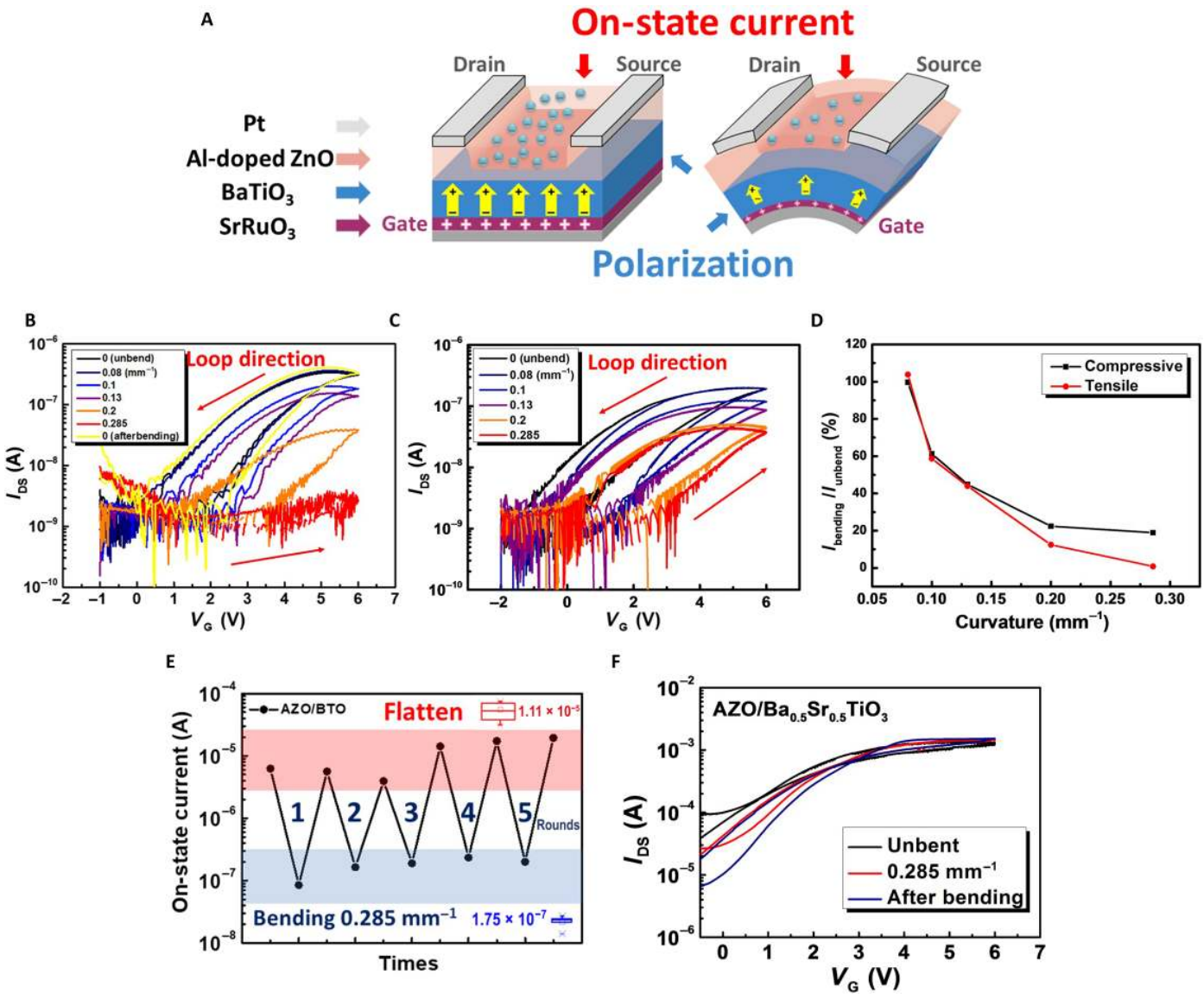

Fig. 4. The characteristics of flexible FeFET. (**A**) Schematic diagram of flexible FeFET. (**B**) Different bending results of I_D-V_G counterclockwise curve under V_G sweeping from −1 to 6 V. (**C**) I_D-V_G counterclockwise curve under compressive bending. (**D**) The ratio of bending and unbend on-state current. (**E**) Five rounds of durability test started after 1000 bending cycles, and the on/off current ratio was two orders of magnitude. (**F**) The I_{DS} of AZO/BSTO transistor shows a neglectable alteration under bending.

layer was grown on top of the BTO layer. This design can convert a simple tunable ferroelectric capacitor to a mechanically controllable transistor. According to the CV and PV measurements, it can be known that the polarization intensity of BTO was gradually weakened under mechanical bending. This behavior should affect the electron concentration in the n-type semiconductor AZO layer, implying a possibility of modulating the source to drain current (I_D) in the AZO layer. The schematic of the device was shown in Fig. 4A. In terms of the electrical measurement, where the I_D was measured under a gate voltage (V_G) from −1 to 6 V with a 3-V drain voltage (V_D). As shown in Fig. 4B, a two-order change on the ratio of on/off current was observed, suggesting that the carriers in the channel can be controlled by the V_G effectively. A counterclockwise I_D-V_G curve hysteresis indicates the ferroelectric conversion behavior from the BTO layer but different to the clockwise curve responsible for flash memory devices. The bending result is also shown in the same figure (Fig. 4A). The I_D started decreasing, while the bending curvature of the heterostructure was varied from 0 to 0.285 mm^{-1}. The drop caused by mechanical bending was about two orders. The on-state current under the opposite bending direction (flex-in) is shown in Fig. 4C. Same as the tensile bending, the decreasing tendency can also be observed under compressive bending. The I_D was measured under the same condition as the flex-out measurement, and the on-state current is changed from 1.92×10^{-7} to 3.64×10^{-8} under 0.285-mm^{-1} curvature. To highlight the decrease of I_D, we recorded the ratio of bending/unbent current, as shown in Fig. 4D. Both compressive and tensile

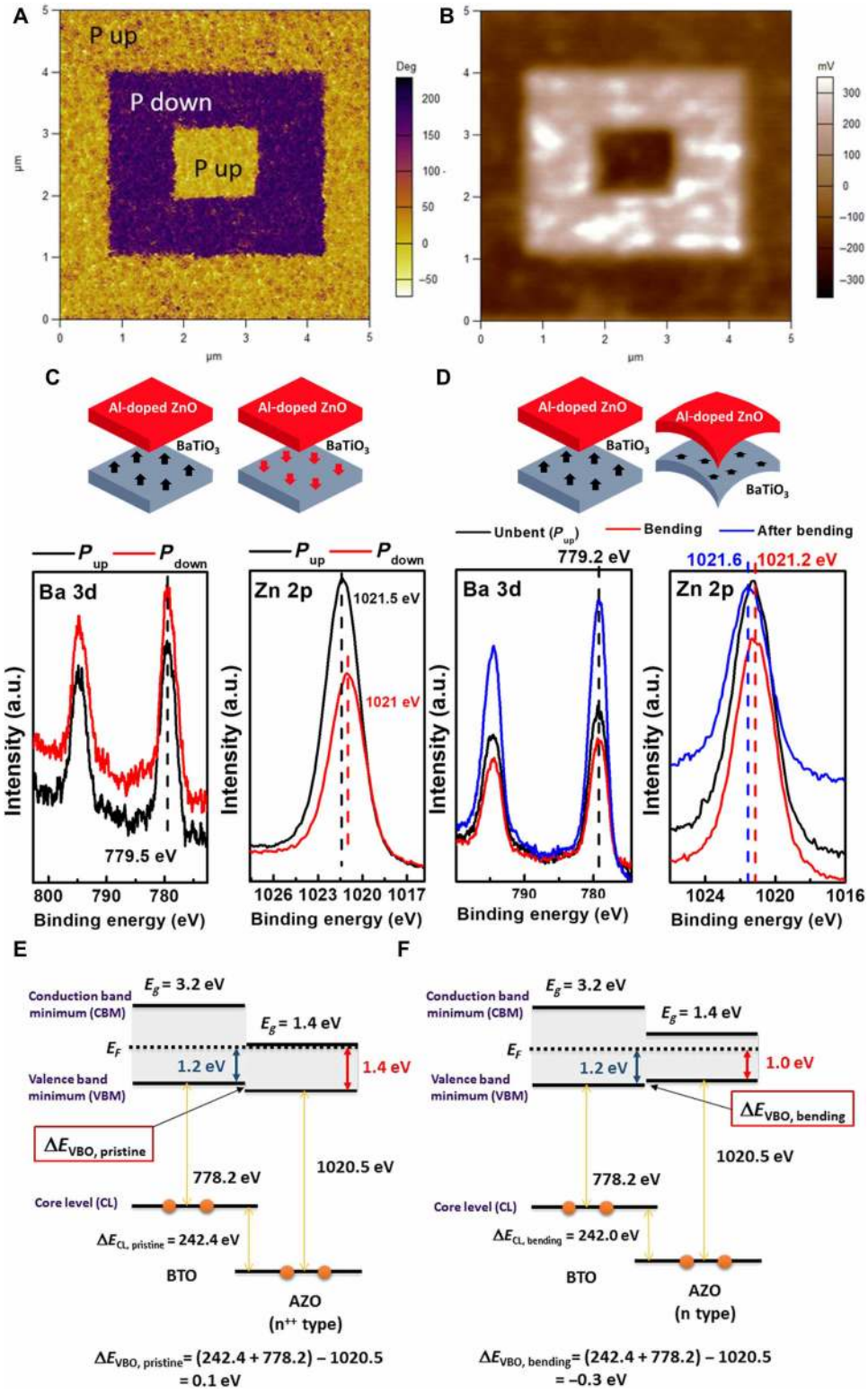

Fig. 5. The scanning probe microscopy under flex-out 0.285-mm^{-1} bending curvature. (**A**) PFM out-of-plane phase after the poling process. (**B**) KPFM surface potential was detected directly after the PFM measurement. The band structure of the FeFET was probed by XPS measurement. (**C**) The Zn 2p and Ba 3d XPS spectra of AZO/BTO sample in the P_{down} and P_{up} states. (**D**) The Zn 2p and Ba 3d XPS spectra of AZO/BTO sample in the unbent, bending, and flattened states. (**E** and **F**) Schematic diagrams illustrating the energy band alignment at the AZO/BTO heterojunction in the unbent and bending states.

bending can decrease the on-state current. However, the strain effect was more obvious under tensile bending. To ensure the reliability of this phenomenon, we performed several rounds of measurements after 1000 bending-flatten cycles, and the result is shown in Fig. 4E. The ratio between the on-state current at the flattened state and the flex-out state with a 0.285-mm^{-1} bending radius remains the same. This result delivers that the flexible FeFET fabricated on a muscovite substrate shows high reliable application value. Last, to confirm that the change of the on-state current is caused by the tunable intensity of the polarization in BTO layer, we also fabricated AZO on a paraelectric BSTO. The I_D-V_G curve is shown in Fig. 4F, and there was no gap in the on-state current between the unbent and bending states in the AZO/BSTO transistor. According to Fig. 4 (B to F), it can be sure that AZO/BTO/SRO/muscovite is a mechanically controllable transistor.

On the basis of the macroscopic evidence, the polarization density of BTO could be manipulated by mechanically bending. In addition, to confirm the local polarization change of BTO layer and the influence on AZO layer, piezoresponse force microscopy (PFM) and Kelvin probe force microscopy (KPFM) were used. In our measurement, we detected the exact same area in the AZO/BTO/SRO/CFO/mica sample to compare the average amplitudes under the flattened state and at the flex-out state with a 0.285-mm^{-1} bending curvature. The details are shown in the Supplementary Materials. To investigate local polarization under the flex-out mode with a 0.285-mm^{-1} bending curvature, we explored the out-of-plane polarization switching pattern by scanning conductive tips as shown in Fig. 5A. The initial poling was carried out by applying a −9-V tip bias on a 5 μm^2 by 5 μm^2 area, followed by applying an +8.6-V tip bias on a concentric 3 μm^2 by 3 μm^2 area, and also followed by applying a −9-V tip bias on a concentric 1 μm^2 by 1 μm^2 area enclosed within the previous one. After the poling process, the local reversal of the BTO polarization direction could be observed by the out-of-plane phase contrast shown in Fig. 5A, although the BTO film is beneath the AZO layer. The topography and amplitude signal were also extracted simultaneously and are shown in the Supplementary Materials. The amplitude in PFM measurement reveals the strength of polarization, which could be further calculated to extract local piezoelectric constant d_{33}. From the average of amplitude signal in the 3 μm^2 by 3 μm^2 area and the relative PFM strength with the standard sample, the calculated local effective d_{33} was about 40.79 pm/V under the flex-out mode with a 3.5-mm bending radius. Note that, in the same area of AZO/BTO/SRO/CFO/mica samples under the flattened circumstance, the average d_{33} was increased to 56.51 pm/V. Evidently, the decrease of average d_{33} value under bending displays the weakening effect on BTO polarization by mechanical bending process, which is consistent with the FeFET results. On the other hand, the charge trapping on surface after poling also displays the same behavior. Figure 5B displays the KPFM results on the flex-out state with a 0.285-mm^{-1} bending curvature measured right after the PFM experiment. The potential change between P_{up} and P_{down} area reflects the injected electron attracted by positive-bound charges in the area of BTO upward polarization. Note that, in n-type AZO, the lowering of energy diagram due to polarization-bound charges causes higher carrier concentration, known as the on-state in FeFET, and the potential difference in KPFM reveals that the carrier concentration transforms between on and off state spatially. Significantly, compared with the flattened condition, we also observed potential difference shrinks under the state with a 0.285-mm^{-1} bending curvature, which shows the shrinkage of carrier concentration (fig. S3). This local KPFM combined with PFM results are again consistent with the electrical measurements, and the surface potential change in AZO is the key to the reduction of the on-state I_D by mechanical bending.

To obtain more insights, the determination of band structure is very crucial. In the heterostructure, the position of the Fermi level in the AZO layer should be modulated by the ferroelectric polarization of BTO layer. Such an effect should change the binding energy of the AZO layer. To acquire the band structure in the heterostructure, we conducted high-resolution XPS in the National Synchrotron Radiation Research Center (NSRRC). The measurement was divided into two parts. In the first part, we investigated the effect of BTO polarization direction on the electronic structure of the AZO layer. Control of the polarization direction of the BTO layer to be up or down was implemented through a poling process by PFM. The binding energies of Zn in the top AZO semiconductor layer and Ba in the ferroelectric BTO layer were measured as shown in Fig. 5C. After the alignment of the Ba binding energy (779.9 eV) in the spectra, the core-level electron (CL) of Zn 2p shows the peaks at 1021.5 and 1021.0 eV in the configurations of up and down polarized BTO layer, respectively. For n-type AZO semiconductor, the rise of Zn 2p binding energy represents the increase of carrier concentration and results in higher conductivity since the Fermi level is shifted closer to the conduction band. As the result, the polarization direction of BTO can change the binding energy of the AZO layer at around 0.5 eV. The second part of the XPS measurement was focused on investigating the change of band structure under the bending test (Fig. 5D). Same as before, the Zn 2p binding energy CL (black line) was 1021.6 eV after an alignment of the Ba binding energy to 779.2 eV. After applying tensile strain to the heterostructure through sticking the heterostructure on the bending stage with a flex-out 0.285-mm^{-1} bending curvature, CL (red line) of the Zn 2p binding energy fell to 1021.2 eV, suggesting a decrease of carrier concentration and a modulation on the conductivity of the AZO layer by mechanical bending. Note that CL of the binding energy of Zn 2p went back to 1021.6 eV (blue line), which is close to the original result when the film was flattened after bending. The ΔE_{VBO} of AZO can be determined according to the above result and is built in schematic diagrams of Fig. 5 (E and F). The ΔE_{VBO} in the unbent state was 0.1 eV and under the bending state was −0.3 eV. The alternation of ΔE_{VBO} was due to the redistribution of charge carriers in the AZO/BTO interface. The as-grown BTO that contained the upward polarization attracts more carriers in AZO than bending so that the value of ΔE_{VBO} decreases by 0.4 eV. This result delivered the evidence on the modulation of AZO semiconductor layer by ferroelectric polarization under mechanical bending.

DISCUSSION

In this work, the flexible oxide heteroepitaxial capacitor and FeFET composed by the paraelectric BSTO, ferroelectric BTO, and semiconducting AZO layers were fabricated on a 2D muscovite substrate with the identification of epitaxial relationship. The BSTO capacitor demonstrated high tunability (−77.8 to 34%) of dielectric constant under mechanical bending. Without the AZO layer, the experiments on BTO/SRO/Mica sample showed a decrease on the magnitude of BTO ferroelectric polarization at different bending radii. In the FeFET part, the ratio of on/off current can reach a two-order-of-magnitude change and exhibit the counterclockwise I_D-V_D curve attributed to the BTO ferroelectricity. When it was bent at a 0.285-mm^{-1} curvature,

the decline was approximately equal to the amount of two orders. The results of XPS and Raman spectroscopy, together with the phase-field simulation, deliver the critical insights of the mechanism. We are confident that the FeFET based on the heteroepitaxy on muscovite can become a flexible and tunable electronic component through simple mechanical bending. This brand new breakthrough provides a promising path for future applications of mechanically tunable technology.

MATERIALS AND METHODS

Sample preparation

Epitaxial BSTO/SRO and AZO/BTO/SRO heterostructures were fabricated on (001) native muscovite substrate using a multitarget laser molecular beam epitaxy system equipped with a high-vacuum chamber up to 10^{-7} torr. The polycrystalline oxide AZO, BSTO, BTO, and SRO targets were prepared by solid-state reaction of powders. Muscovite (001) substrates were ultrasonically cleaned in acetone, methanol, isopropyl alcohol, and deionized water. The cleaned substrate was loaded into the processing chamber immediately to minimize possible contaminations. A KrF excimer laser (λ = 248 nm; Lambda Physik) was operated at a 10-Hz repetition rate and energy density of 1 J/cm^2. The deposition process was carried out in the condition of 110 mtorr and 300°C for 50 nm of AZO, 100 mtorr and 720°C for 200 nm of BTO and 400 nm of BSTO, 80 mtorr and 680°C for 100 nm of SRO, and 50 mtorr and 650°C for 20 nm of CFO. Last, Pt film was then deposited at room temperature and patterned into the source/drain electrodes by radiofrequency sputter method.

Bending measurements

A strict packaging process that can fix this flexible electrical component tightly on the brass-made bending stage to confirm the strain was directly applied to the heterostructure. During the bending measurement, any optical cracks and wrinkles were not allowed to appear on the surface of the heterostructures. In this study, a glue was used to seal the edges of the heterostructures, providing a strong connection of the heterostructure. This is the key to impose the strain to the heterostructure. The schematic diagram of fixed edge and loose edge under bending measurement is shown in fig. S4.

X-ray diffraction

XRD experiments were performed on the Bruker D8 Discover XRD System, which uses Cu K_α x-ray to obtain the 2θ-θ scan along normal direction and the Φ-scans at room temperature.

Transmission electron microscopy

The films-substrate interface microstructure was observed by field emission TEM. Cross-sectional samples were prepared by a standard ion-milling technique. Microstructural investigations were done on a JEOL JEM-F200.

Electrical properties

The electrical characterization was performed in a physical property measurement system (Quantum Design). The relative dielectric constant and ferroelectric properties of the BTO thin films were analyzed from −2 to 2 V with 100 mV of alternating voltage (AV) frequency and 100 kHz of AC frequency using a semiconductor analyzer (B1500A, Agilent Technologies) under room temperature. The PV measurement was performed under 100 mV of AV voltage, 5 kHz of AC frequency, and the voltage was measured from 30 to −30 V. The current-voltage properties of the flexible ferroelectric transistor were measured through a semiconductor parameter analyzer (B1500A, Agilent Technologies). High thermal conductivity double-sided copper tape was used to adhere the heterostructures on the copper-bending platform and measure the alterations of Curie point.

Raman scattering

The variable temperature Raman spectra were captured by a confocal backscattering-based detection in ambient environment with a spectrometer (iHR550, HORIBA Jobin Yvon) and a 532-nm solid-state laser as the excited source (in continuous operation). A 100× objective lens (numerical aperture = 0.95) was used with a focused spot size ~3 μm^2. The Raman spectra resolution is ~0.74 cm^{-1}. The bending measurement Raman spectra was measured by DXR2 Raman Microscope (Thermo Fisher Scientific) with 532-nm solid-state laser.

Phase-field simulations

Phase-field simulations are carried out in 80 nm by 80 nm by 20 nm film regions. Short-circuit boundary conditions (i.e., Dirichlet's boundary conditions) are applied to both top and bottom surfaces to solve the electrostatic equation. When solving the mechanical equilibrium equation, the top surface is set as mechanically free, and the bottom surface is fixed. The simulations are carried out with finite element method implemented in a COMSOL Multiphysics software kit.

To model the (111)-oriented film, two coordinate systems are involved: $\boldsymbol{x}'(x', y', z')$ is the coordinate system extending along the film plane and the film normal, in which all components of a vector is represented with a prime, and $\boldsymbol{x}(x, y, z)$ is the coordinate system extending along the crystal directions $[100]_c$, $[010]_c$, and $[001]_c$. Spatial and temporal evolutions of polarization are governed by the time-dependent Landau-Ginzburg equation (*33*)

$$\frac{\partial P_i(\boldsymbol{x})}{\partial t} = -L\frac{\delta F}{\delta P_i(\boldsymbol{x})} \tag{2}$$

Where L is the kinetic coefficient, and P_i is the ith component of polarization in the $\boldsymbol{x}$ coordinate system. The total free energy F is written as

$$F\int_V (f_{\text{Landau}} + f_{\text{grad}} + f_{\text{elec}} + f_{\text{elas}})\ \mathrm{d}V \tag{3}$$

Where f_{Landau}, f_{grad}, f_{elec}, and f_{elas} represent the Landau, polarization gradient, electric, and elastic energy densities, respectively. The Landau energy is given by the Landau polynomial

$$\begin{aligned} f_{\text{Landau}} &= a_1\left(P_1^2P_2^2 + P_3^2\right) + \alpha_{11}\left(P_1^4 + P_2^4P_3^4\right) + \alpha_{12}\left(P_1^2P_2^2 + P_2^2P_3^2 + P_3^2P_1^2\right) \\ &+ \alpha_{123}P_1^2P_2^2P_3^2 + \alpha_{111}\left(P_1^6 + P_2^6 + P_3^6\right) \\ &+ \alpha_{112}\left[P_1^2\left(P_2^4 + P_3^4\right) + P_2^2\left(P_3^4 + P_1^4\right) + P_3^2\left(P_1^4P_2^4\right)\right] + \alpha_{1111}\left(P_1^8 + P_2^8 + P_3^8\right) \\ &+ \alpha_{1112}\left[P_1^6\left(P_2^2 + P_3^2\right) + P_2^6\left(P_3^2 + P_1^2\right) + P_3^6\left(P_1^2 + P_2^2\right)\right] \\ &+ \alpha_{1122}\left(P_1^4P_2^4 + P_2^4P_3^4 + P_3^4P_1^4\right) + \alpha_{1123}\left(P_1^4P_2^2P_3^2 + P_2^4P_3^2P_1^2 + P_3^4P_1^2P_2^2\right) \end{aligned} \tag{4}$$

where α_1, α_{11}, α_{12}, α_{111}, α_{112}, α_{123}, α_{1111}, α_{1112}, α_{1122}, and α_{1123} are Landau coefficients of $Ba_{(1-x)}Sr_xTiO_3$ (*34*). These coefficients are composition dependent; therefore, BSTO and BTO films could be modeled with the same infrastructure.

With Einstein's notation, which requires summation over all possible values of indices appeared in pairs, the elastic energy density is written as

$$f_{\text{elas}} = \frac{1}{2}(\epsilon_{ij} - \epsilon_{ij}^{0})\, C_{ijkl}(\epsilon_{kl} - \epsilon_{kl}^{0}) \quad (5)$$

Where ϵ_{ij} is the total strain. The eigenstrain ϵ_{ij}^{0} describes the relative lattice parameter changes during ferroelectric phase transition under the stress-free boundary condition. The local eigenstrain is related to local polarization through $\epsilon_{ij}^{0}(x) = Q_{ijkl} P_k(x) P_l(x)$ with the electrostrictive coefficients Q_{ijkl} representing the degree of coupling between the polarization and the lattice degrees of freedom in ferroelectrics. The electric energy density is given by

$$f_{\text{elec}} = -\frac{1}{2}\kappa\varepsilon_0 E^2 - P_i E_i \quad (6)$$

Where E is the electric field and κ is the background dielectric constant. The gradient energy density is

$$f_{\text{grad}} = G_{ijkl} \frac{\partial P_i'}{\partial x_j} \frac{\partial P_k'}{\partial x_l} \quad (7)$$

Where G_{ijkl} are gradient energy coefficients.

PFM and KPFM

PFM and KPFM results were obtained by an MFP-3D scanning probe microscope (SPM) system (Asylum Research, CA, USA) with typical conductive tips (Olympus OSCM-PIT, Pt/Ir coating; f = 60 to 100 kHz, k = 1 to 5 N/m). The dimensions of the tip such as its stiffness, radius, and sharpness are significant to high-resolution SPM studies (*35*–*36*). To increase the PFM signal-to-noise ratio, we used dual AC resonance tracking method (*37*), and the tip was driven by an AC voltage of 1 V at each PFM measurement (contact resonance frequency ≈ 250 kHz).

X-ray photoelectron spectroscopy

XPS is a powerful tool to in situ–probe the electronic structure of AZO/BTO nanostructure. A commercial "SPECS PHOIBOS 150 analyzer" is used to measure the XPS spectra. Measurements were performed at the NSRRC in Hsinchu, Taiwan at photon energies of 1487 eV. All measurements were carried out at room temperature.

SUPPLEMENTARY MATERIALS

Supplementary material for this article is available at http://advances.sciencemag.org/cgi/content/full/6/10/eaaz3180/DC1

Fig. S1. BSTO structure properties.
Fig. S2. The detailed analysis of Raman spectra.
Fig. S3. PFM and KFPM results.
Fig. S4. The different results of 2D muscovite under bending.

REFERENCES AND NOTES

1. F. Segovia-Chaves, H. Vinck-Posada, E. Navarro-Barón, Dependence on hydrostatic pressure in two-dimensional triangular photonic crystals. *Physica B* **557**, 88–94 (2019).
2. T. Yagi, Y. Ida, Y. Sato, S.-I. Akimoto, Effect of hydrostatic pressure on the lattice parameters of Fe_2SiO_4 olivine up to 70 kbar. *Phys. Earth Planet. Int.* **10**, 348–354 (1975).
3. J. Du, Z. Yang, X. Xu, X. Wang, X. Du, Effects of tea polyphenols on the structural and physicochemical properties of high-hydrostatic-pressure-gelatinized rice starch. *Food Hydrocoll.* **91**, 256–262 (2019).
4. Y. Lia, H. Wang, Y. Yao, J. Xu, Z. Han, Y. Fang, L. Zhang, C. Zhang, B. Qian, X. Jiang, Magnetic phase diagram, magnetocaloric effect, and exchange bias in $Ni_{43}Mn_{46}Sn_{11-x}Ga_x$ Heusler alloys. *J. Magn. Magn. Mater.* **478**, 161–169 (2019).
5. A. Wójcika, W. Maziarz, M. J. Szczerba, M. Sikora, A. Żywczak, C. O. Aguilar-Ortiz, P. Álvarez-Alonso, E. Villa, H. Flores-Zúñiga, E. Cesari, J. Dutkiewicz, V. A. Chernenko, Transformation behavior and inverse caloric effects in magnetic shape memory $Ni_{44-x}Cu_xCo_6Mn_{39}Sn_{11}$ ribbons. *J. Alloy. Compd.* **721**, 172–181 (2017).
6. A. Sozinov, A. A. Likhachev, N. Lanska, K. Ullakko, Giant magnetic-field-induced strain in NiMnGa seven-layered martensitic phase. *Appl. Phys. Lett.* **80**, 1746–1748 (2002).
7. H. Fu, R. E. Cohen, Polarization rotation mechanism for ultrahigh electromechanical response in single-crystal piezoelectrics. *Nature* **403**, 281–283 (2000).
8. J. X. Zhang, B. Xiang, Q. He, J. Seidel, R. J. Zeches, P. Yu, S. Y. Yang, C. H. Wang, Y.-H. Chu, L. W. Martin, A. M. Minor, R. Ramesh, Large field-induced strains in a lead-free piezoelectric material. *Nat. Nanotechnol.* **6**, 98–102 (2011).
9. B. Kundys, Photostrictive materials. *Appl. Phys. Rev.* **2**, 011301 (2015).
10. Y. Li, L. Meng, Y. M. Yang, G. Xu, Z. Hong, Q. Chen, J. You, G. Li, Y. Yang, Y. Li, High-efficiency robust perovskite solar cells on ultrathin flexible substrates. *Nat. Commun.* **7**, 10214 (2016).
11. C. T. Avedisian, R. E. Cavicchi, P. M. McEuen, X. Zhou, W. S. Hurst, J. T. Hodges, High temperature electrical resistance of substrate-supported single walled carbon nanotubes. *Appl. Phys. Lett.* **93**, 252108 (2008).
12. C.-H. Ma, J.-C. Lin, H.-J. Liu, T. H. Do, Y.-M. Zhu, T. D. Ha, Q. Zhan, J.-Y. Juang, Q. He, E. Arenholz, P.-W. Chiu, Y.-H. Chu, Van der Waals epitaxy of functional MoO_2 film on mica for flexible electronics. *Appl. Phys. Lett.* **108**, 253104 (2016).
13. J. A. DeRose, T. Thundat, L. A. Nagahara, S. M. Lindsay, Gold grown epitaxially on mica: Conditions for large area flat faces. *Surf. Sci.* **256**, 102–108 (1991).
14. T. Yang, B. Zheng, Z. Wang, T. Xu, C. Pan, J. Zou, X. Zhang, Z. Qi, H. Liu, Y. Feng, W. Hu, F. Miao, L. Sun, X. Duan, A. Pan, Van der Waals epitaxial growth and optoelectronics of large-scale WSe2/SnS2 vertical bilayer p–n junctions. *Nat. Commun.* **8**, 1906 (2017).
15. J. Kim, C. Bayram, H. Park, C. W. Cheng, C. Dimitrakopoulos, J. A. Ott, K. B. Reuter, S. W. Bedell, D. K. Sadana, Principle of direct van der Waals epitaxy of single-crystalline films on epitaxial graphene. *Nat. Commun.* **5**, 4836 (2014).
16. L. Tang, C. Teng, Y. Luo, U. Khan, H. Pan, Z. Cai, Y. Zhao, B. Liu, H. M. Cheng, Confined van der Waals epitaxial growth of two-dimensional large single-crystal In_2Se_3 for flexible broadband photodetectors. *Research* **2019**, 2763704 (2019).
17. C. Ederer, N. A. Spaldin, Effect of epitaxial strain on the spontaneous polarization of thin film ferroelectrics. *Phys. Rev. Lett.* **95**, 257601 (2005).
18. H. Yu, C.-C. Chung, N. Shewmon, S. Ho, J. H. Carpenter, R. Larrabee, T. Sun, J. L. Jones, H. Ade, B. T. O'Connor, F. So, Flexible inorganic ferroelectric thin films for nonvolatile memory devices. *Adv. Funct. Mater.* **27**, 1700461 (2017).
19. J. Lyu, I. Fina, R. Solanas, J. Fontcuberta, F. Sánchez, Tailoring lattice strain and ferroelectric polarization of epitaxial $BaTiO_3$ thin films on Si(001). *Sci. Rep.* **8**, 495 (2018).
20. K. J. Choi, M. Biegalski, Y. L. Li, A. Sharan, J. Schubert, R. Uecker, P. Reiche, Y. B. Chen, X. Q. Pan, V. Gopalan, L. Q. Chen, D. G. Schlom, C. B. Eom, Enhancement of ferroelectricity in strained $BaTiO_3$ thin films. *Science* **306**, 1005–1009 (2004).
21. J. H. Haeni, P. Irvin, W. Chang, R. Uecker, P. Reiche, Y. L. Li, S. Choudhury, W. Tian, M. E. Hawley, B. Craigo, A. K. Tagantsev, X. Q. Pan, S. K. Streiffer, L. Q. Chen, S. W. Kirchoefer, J. Levy, D. G. Schlom, Room-temperature ferroelectricity in strained $SrTiO_3$. *Nature* **430**, 758–761 (2004).
22. Y. Kaneko, H. Tanaka, M. Ueda, Y. Kato, E. Fujii, A dual-channel ferroelectric-gate field-effect transistor enabling nand -type memory characteristics. *IEEE Trans. Electron Devices* **58**, 1311–1318 (2011).
23. I. Katsouras, D. Zhao, M.-J. Spijkman, M. Li, P. W. M. Blom, D. M. de Leeuw, K. Asadi, Controlling the on/off current ratio of ferroelectric field-effect transistors. *Sci. Rep.* **5**, 12094 (2015).
24. H. Mulaosmanovic, E. Chicca, M. Bertele, T. Mikolajickac, S. Slesazecka, Mimicking biological neurons with a nanoscale ferroelectric transistor. *Nanoscale* **10**, 21755–21763 (2018).
25. R. Kant, C. Dwivedi, S. Pathak, V. Dutta, Fabrication of ZnO nanostructures using Al doped ZnO (AZO) templates for application in photoelectrochemical water splitting. *Appl. Surf. Sci.* **447**, 200–212 (2018).
26. Z. Hu, Z. Deng, Q. Wei, T. Zhao, Y. Wang, Z. Yu, L. Ma, K. Zhou, Roles of Al-doped ZnO (AZO) modification layer on improving electrochemical performance of $LiNi_{1/3}Co_{1/3}Mn_{1/3}O_2$ thin film cathode. *Ionics* **23**, 2981–2992 (2017).
27. J.-T. Luo, A.-J. Quan, Z.-H. Zheng, G.-X. Liang, F. Li, A.-H. Zhong, H.-L. Ma, X.-H. Zhang, P. Fan, Study on the growth of Al-doped ZnO thin films with (11$\bar{2}$0) and (0002) preferential orientations and their thermoelectric characteristics. *RSC Adv.* **8**, 6063–6068 (2018).
28. H.-J. Liu, C.-K. Wang, D. Su, T. Amrillah, Y.-H. Hsieh, K.-H. Wu, Y.-C. Chen, J.-Y. Juang, L. M. Eng, S.-U. Jen, Y.-H. Chu, Flexible heteroepitaxy of $CoFe_2O_4$/muscovite bimorph with large magnetostriction. *ACS Appl. Mater. Interfaces* **9**, 7297–7304 (2017).
29. A. Tombak, J.-P. Maria, F. Ayguavives, Z. Jin, G. T. Stauf, A. I. Kingon, A. Mortazawi, Tunable barium strontium titanate thin film capacitors for RF and microwave applications. *IEEE Microw. Wirel. Compon. Lett.* **12**, 3–5 (2002).

30. H. Hayashi, T. Nakamura, T. Ebina, In-situ Raman spectroscopy of $BaTiO_3$ particles for tetragonal–cubic transformation. *J. Phys. Chem. Solid* **74**, 957–962 (2013).
31. B. Wang, L. D. Zhang, L. Zhang, Y. Yan, S. L. Zhang, Raman scattering from $BaTiO_3$ thin film prepared on silicon substrate by r.f. sputtering. *Thin Solid Films* **354**, 262–266 (1999).
32. J.-J. Wang, B. Wang, L.-Q. Chen, Understanding, predicting, and designing ferroelectric domain structures and switching guided by the phase-field method. *Annu. Rev. Mat. Res.* **49**, 127–152 (2019).
33. J. J. Wang, X. Q. Ma, Q. Li, J. Britson, L.-Q. Chen, Phase transitions and domain structures of ferroelectric nanoparticles: Phase field model incorporating strong elastic and dielectric inhomogeneity. *Acta Mater.* **61**, 7591–7603 (2013).
34. Y. H. Huang, J. J. Wang, T. N. Yang, Y. J. Wu, X. M. Chen, L. Q. Chen, A thermodynamic potential, energy storage performances, and electrocaloric effects of $Ba_{1-x}Sr_xTiO_3$single crystals. *Appl. Phys. Lett.* **112**, 102901 (2018).
35. C. Musumeci, A. Liscio, V. Palermo, P. Samorì, Electronic characterization of supramolecular materials at the nanoscale by Conductive Atomic Force and Kelvin Probe Force microscopies. *Mater. Today* **17**, 504–517 (2014).
36. G. H. Enevoldsen, T. Glatzel, M. C. Christensen, J. V. Lauritsen, F. Besenbacher, Atomic scale kelvin probe force microscopy studies of the surface potential variations on the TiO_2(110) surface. *Phys. Rev. Lett.* **100**, 236104 (2008).
37. J. R. Brian, C. Clint, V. K. Sergei, P. Roger, Dual-frequency resonance-tracking atomic force microscopy. *Nanotechnology* **18**, 475504 (2007).

Acknowledgments: We thank the cooperation of the simulation team. **Funding:** This work is supported by Ministry of Science and Technology, Taiwan (grant nos. MOST 106-2119-M-009-011-MY3, 106-2628-E-009-001-MY2, 106-2218-E-009-021, 106-2923-M-009-003-MY2, 107-2112-M-001-042-MY3, and 107-2218-E-007-050) and the Center for Emergent Functional Matter Science of National Chiao Tung University from The Featured Areas Research Center Program within the framework of the Higher Education Sprout Project by the Ministry of Education (MOE) in Taiwan. Y.Z.T. acknowledges the support from Pennsylvania State MRSEC, Center for Nanoscale Science, under the award NSF DMR-1420620. J.J.W. acknowledges the support from the Army Research Office under grant number W911NF-17-1-0462. L.-Q.C. acknowledges the support from NSF under grant number DMR-1744213 and the Donald W. Hamer Foundation through a Hamer Professorship at Penn State. **Author contributions:** M.F.T. assisted in the construction of FeFET structure. J.W.C. obtained the XPS result. P.W.S. assisted in the data collection of SPM system. Y.Z.T. and J.J.W. helped with the calculation of simulation part. S.Z.H. polled the sample before the XPS measurement. Y.H.L. contained the TEM result. D.P.T. provided the SPM system and is currently with Department of Electronic and Information Engineering, Hong Kong Polytechnic University. Y.L.C. provided the electrical measurement equipment. Y.C.C. analyzed the Raman result. L.-Q.C. designed the simulation. Y.H.C. directed the project, designed experiments, analyzed data, and assisted in writing the manuscript. All authors discussed the results and commented on the manuscript. **Competing interests:** The authors declare that they have no competing interests. **Data and materials availability:** All data needed to evaluate the conclusions in the paper are present in the paper and/or the Supplementary Materials. Additional data related to this paper may be requested from the authors.

Submitted 29 August 2019
Accepted 12 December 2019
Published 6 March 2020
10.1126/sciadv.aaz3180

Citation: D. L. Ko, M. F. Tsai, J. W. Chen, P. W. Shao, Y. Z. Tan, J. J. Wang, S. Z. Ho, Y. H. Lai, Y. L. Chueh, Y. C. Chen, D. P. Tsai, L.-Q. Chen, Y. H. Chu, Mechanically controllable nonlinear dielectrics. *Sci. Adv.* **6**, eaaz3180 (2020).

ScienceAdvances

Mechanically controllable nonlinear dielectrics

D. L. KoM. F. TsaiJ. W. ChenP. W. ShaoY. Z. TanJ. J. WangS. Z. HoY. H. LaiY. L. ChuehY. C. ChenD. P. TsaiL.-Q. ChenY. H. Chu

Sci. Adv., 6 (10), eaaz3180.

Science Advances (ISSN 2375-2548) is published by the American Association for the Advancement of Science. 1200 New York Avenue NW, Washington, DC 20005. The title *Science Advances* is a registered trademark of AAAS.